
3 Local Field Potentials

Biophysical Origin and Analysis

*Gaute T. Einevoll, Henrik Lindén, Tom Tetzlaff,
Szymon Łęski, and Klas H. Pettersen*

CONTENTS

3.1	Introduction	37
3.2	Biophysical Origin	38
3.3	Single-Neuron LFP	40
3.4	Population LFP	44
3.4.1	Model for Population LFP	44
3.4.2	Analytical Formulas for Summation of Population LFP	45
3.4.2.1	Uncorrelated LFP Sources	46
3.4.2.2	Correlated LFP Sources	48
3.4.3	Decay of LFP Outside Neuronal Population	48
3.5	Analysis of LFP Data	50
3.5.1	Current-Source Density (CSD)	50
3.5.2	Current-Source Density (CSD) Analysis	51
3.5.2.1	Traditional CSD Analysis	51
3.5.2.2	Inverse CSD Analysis	52
3.5.2.3	Other CSD Analysis Methods Based on Forward Model	53
3.5.3	Interpretation in Terms of Neuronal Populations	54
3.6	Concluding Remarks	55
	Acknowledgments	56
	References	56

3.1 INTRODUCTION

The previous chapter focused on the biophysics of generation of spikes, the extracellular signature of action potentials, representing the output of the computation done by individual neurons. In this chapter, we focus on the generation of local field potentials (LFPs), which in contrast appears to predominantly reflect the synaptic inputs to the neurons. The measurement of LFPs, which we here define as the low-frequency part of the electrical potential recorded by an extracellular electrode inserted into the brain, is among the oldest techniques for studying neural activity. Already in 1875, Richard Caton could report that he had measured electrical signals from the cortical surface of living animals (Caton 1875), 50 years before the first EEG was recorded (Berger 1929). As the LFP stems from activity in populations of neurons around the electrode, the signal is not straightforward to interpret. Early investigators thus focused on the high-frequency part of the signal, the multi-unit activity (MUA), which contains information about the firing of action potentials of a handful of the surrounding neurons (Adrian and Moruzzi 1939). LFP signal revived in the 1950s with the introduction of current-source density (CSD) analysis of multiple LFP recordings across well-organized layered neural structures such as cortex, cerebellum, and hippocampus (Pitts 1952). As the CSD is

a more local measure of neural activity than the LFP (Nicholson and Freeman 1975, Pettersen et al. 2006), it is easier to interpret in terms of the activity in the underlying neural circuits. A comprehensive review of the findings from such CSD analysis in the ensuing three decades can be found in Mitzdorf (1985).

Following an apparent slump in interest, probably due to increased focus on single-neuron properties after the introduction of patch-clamp recording and other new techniques, the interest in LFP has grown over the last decade. One important reason is the development of new silicon-based multielectrodes allowing for simultaneous recording of LFP signals at tens, hundreds, and even thousands of positions (Normann et al. 1999, Buzsaki 2004, Frey et al. 2009, Lambacher et al. 2011, Leski et al. 2011). Further, unlike spikes, the LFP inherently reflects activity at the population level, and it has thus been used to investigate network mechanisms involved in sensory processing (Di et al. 1990, Kandel and Buzsaki 1997, Schroeder et al. 1998, Schroeder et al. 2001, Henrie and Shapley 2005, Einevoll et al. 2007, Belitski et al. 2008, Montemurro et al. 2008, Szymanski et al. 2009), motor planning (Scherberger et al. 2005, Roux et al. 2006), and higher cognitive processes, including attention, memory, and perception (Pesaran et al. 2002, Kreiman et al. 2006, Liu et al. 2006, Womelsdorf et al. 2006, Montgomery and Buzsaki 2007, Colgin et al. 2009). In addition, the LFP has been suggested as a candidate signal for steering motor prosthetic devices (Mehring et al. 2003, Andersen et al. 2004, Rickert et al. 2005) as it is relatively easy to record and more stable than single-unit spiking activity.

Another key development is the adaptation of a biophysical forward-modeling scheme for extracellular potentials (Rall 1962) to incorporate detailed reconstructed neuronal morphologies and thus allow for detailed predictions of the position dependence of recorded extracellular potentials induced by various kinds of neural activity (Holt and Koch 1999). While first used to investigate spikes, the extracellular signatures of action potentials (Holt and Koch 1999, Gold et al. 2006, 2007, Pettersen and Einevoll 2008), the scheme has more recently also been used to calculate LFPs generated by synaptic activation of single neurons (Linden et al. 2010) and population of neurons (Einevoll et al. 2007, Pettersen et al. 2008, Linden et al. 2011, Hagen et al. 2011). This is a crucial advance as it allows for a systematic investigation of the link between the recorded LFP and the underlying neural activity, and thus also a much better foundation for developing and validating methods for the analysis of LFP signals (Pettersen et al. 2006, 2008, Leski et al. 2011, Gratiy et al. 2011).

One of the focus of this chapter will be on the biophysical origin of population LFP, that is, how the LFP from a population of activated neurons is formed by summing LFP contributions from numerous individual neurons. A second focus will be on methods for the analysis of LFP data, in particular CSD analysis, and how the biophysical forward-modeling scheme has been used both for development and validation of such methods. The biophysical origin of LFP and the forward-modeling scheme are described in Section 3.2. In Section 3.3 the scheme is used to investigate the LFP from a single synaptically activated neuron, and in Section 3.4 the formation of population LFPs from the concerted action of many such single-neuron contributions are described. Section 3.5 outlines CSD analysis and other methods for analysis of LFP signals, while some concluding remarks are given in Section 3.6.

3.2 BIOPHYSICAL ORIGIN

The biophysical origin of the LFP seems well established: it is set up by transmembrane currents in cells, predominantly neurons, located in the vicinity of the extracellular electrode (Rall 1962, Nicholson and Freeman 1975). In the commonly used *volume conductor theory* the system is further envisioned as a three-dimensional smooth extracellular continuum described by its electrical conductivity σ_{ex} with transmembrane currents acting as *volume current sources* setting up the extracellular potentials (Nunez and Srinivasan 2006). In this theory the fundamental formula for the contribution to the extracellular potential $\phi(\mathbf{r}, t)$ from the activity of an N -compartment neuron

model is given by (Holt and Koch 1999, Pettersen and Einevoll 2008, Pettersen et al. 2008, Linden et al. 2010)

$$\phi(\mathbf{r}, t) = \frac{1}{4\pi\sigma_{ex}} \sum_{n=1}^N \frac{I_n(t)}{|\mathbf{r} - \mathbf{r}_n|}, \quad (3.1)$$

see Figure 3.1. Here $I_n(t)$ denotes the transmembrane current in compartment n positioned at \mathbf{r}_n , and σ_{ex} is the extracellular conductivity.

This formula relies on a set of assumptions and approximations: The first is the use of the so-called *quasistatic approximation* of Maxwell's equations, where the electrical and magnetic fields are effectively decoupled (Hamalainen et al. 1993). This approximation seems well fulfilled for the frequencies inherent in neural activity, that is, frequencies less than a few thousand hertz (Hamalainen et al. 1993). The formula further assumes an infinite volume conductor where the electrical conductivity σ_{ex} is (1) *ohmic*, that is, no imaginary part of σ_{ex} (Nunez and Srinivasan 2006, Logothetis et al. 2007), (2) *frequency-independent* (Logothetis et al. 2007), (3) *homogeneous* (Goto et al. 2010), and (4) *isotropic* (Logothetis et al. 2007, Goto et al. 2010), that is, the same in all directions. As discussed in Pettersen et al. (2012), however, the biophysical forward-modeling scheme can straightforwardly be generalized to incorporate situations where one or more of these assumptions are unfulfilled. For example, in cortex it has been observed that the electrical conductivity is up to a factor 2 larger in the vertical direction (perpendicular to the cortical surface) than in the lateral direction (Goto et al. 2010), and this can be incorporated by a slight modification

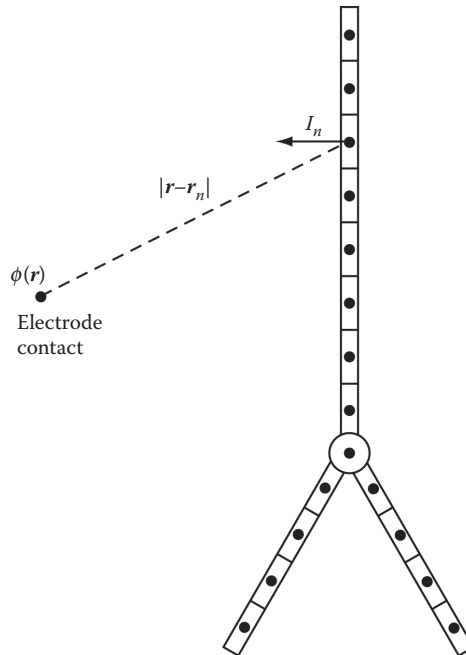


FIGURE 3.1 Illustration of Equation 3.1 providing the link between transmembrane currents I_n and the extracellular potential ϕ . The scheme works for neuronal morphologies of arbitrary complexity, not only simple ball-and-stick neurons as depicted here. In many practical applications the *line-source approximation* has been used (Holt and Koch 1999, Gold et al. 2006, Pettersen and Einevoll 2008, Pettersen et al. 2008, Linden et al. 2010). Here the transmembrane currents are evenly distributed across each linear dendritic segment, and Equation 3.1 is adapted accordingly. Note that the forward-modeling problem also can be formulated in a quite different way by means of surface potentials, see Avitan et al. (2009).

of Equation 3.1 (Nicholson and Freeman 1975). The effect of changes in extracellular conductivity at the top and bottom of cortex, and also at layer boundaries inside cortex, can be incorporated by the “method of images” from electrostatics (Nicholson and Llinas 1971, Pettersen et al. 2006, Goto et al. 2010). Further, in situations with complicated spatial variation of the extracellular conductivities, for example in models where the detailed shape and design of the recording electrodes are included, the forward modeling can be done using finite-element modeling (FEM) of the corresponding Poisson equation (Frey et al. 2009, Mechler and Victor 2011). This is more complicated and demanding in terms of computer power compared to use of direct formulas of the type in Equation 3.1, however.

Q5

3.3 SINGLE-NEURON LFP

In Figure 3.2, we use the forward-modeling scheme described above to highlight some key qualitative features of the contribution to the LFP from individual neurons. Here a layer-5 model pyramidal neuron from cat visual cortex (Mainen and Sejnowski 1996) receives either a single excitatory synaptic current in the apical dendrite (panel a) or a single inhibitory synaptic current of the same size and duration in the soma (panel b). The resulting extracellular potential traces are shown for a set of positions in the vicinity of the neuron revealing that while the largest LFP responses are

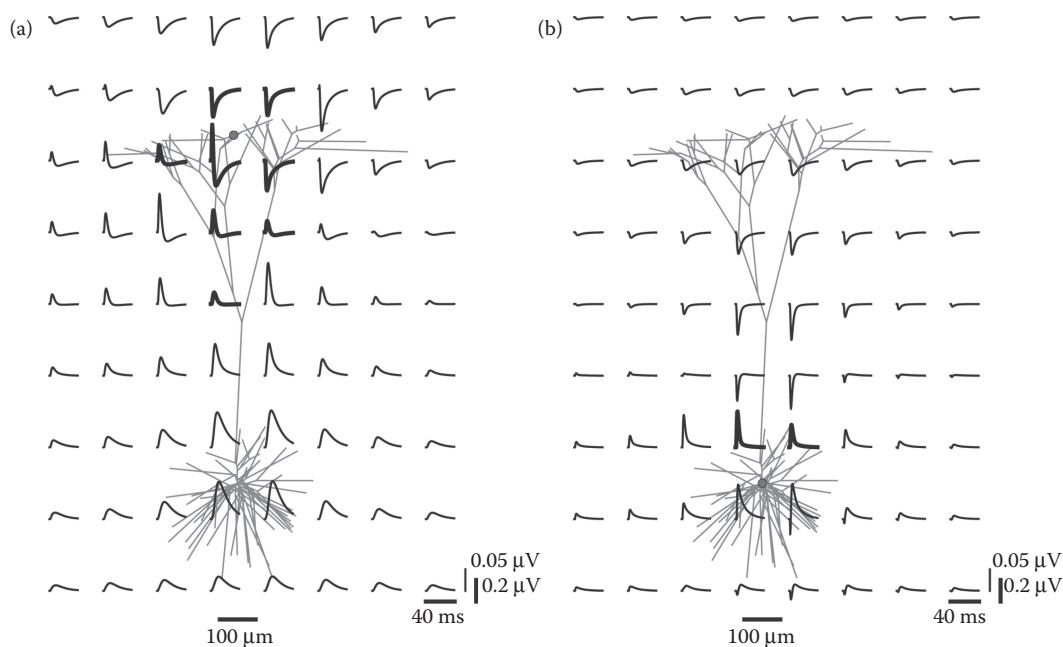


FIGURE 3.2 Calculated extracellular potentials following single synaptic inputs into a purely passive pyramidal neuron model adapted from the reconstructed layer-5 pyramidal neuron used in Mainen and Sejnowski (1996). The line-source approximation and the accordingly adapted version of Equation 3.1 is used (Holt and Koch 1999, Pettersen and Einevoll 2008). (a) Excitatory input to apical dendrite. (b) Inhibitory input to soma. The synapse is current-based (making the model fully linear) and the current magnitude modeled as an α -function $I_s(t) = I_0 t / \tau_s \exp(1 - t / \tau_s)$ for $t > 0$ with $\tau_s = 1$ ms. The magnitude of the constant I_0 is in both cases set to 1 nA which gives a peak EPSP amplitude in the soma of 1.3 mV for the situation in panel A, and an IPSP amplitude of 6.2 mV in B. Passive neuron parameters: membrane resistivity $R_m = 30,000 \Omega \text{ cm}^2$, axial resistivity $R_i = 150 \Omega \text{ cm}$, membrane capacitance $C_m = 1.0 \mu\text{F}/\text{cm}^2$. Extracellular conductivity σ_{ex} is set to 0.3 S/m (Hamalainen et al. 1993). Synapse position is shown as a filled dot.

seen close to the synapse, sizable contributions can also be seen a millimeter away. Further, both the shape and size of the contribution to the LFP vary strongly with position: close to the excitatory synaptic input in panel a the LFP contribution is predominantly negative, reflecting that the synaptic current into the neuron, that is, a current *sink*, dominates the sum in Equation 3.1. For the inhibitory synapse in panel b, the situation is opposite: here a synaptic current *source* dominates the sum for positions close to the synapse giving a predominantly positive contribution to the LFP signal. The two situations depicted in panels a and b will thus have qualitative similar LFP polarity patterns with predominantly negative LFPs around the apical dendrites and positive LFPs around the basal dendrites.

The LFPs of the two situations in Figure 3.2a and b are, however, distinguishable by their frequency content. While the LFP generated by the basal inhibitory input in panel b gives a sharp positive LFP trace below the soma, the apical excitation in panel a gives a more blunted LFP shape. Thus, the LFP in the former case contains more high-frequency components than in the latter. This feature can be understood on the basis of passive cable properties of the neuron: the transmembrane currents dominating the LFP close to the soma in panel a have been low-pass filtered and have a more blunted temporal profile compared to the transmembrane currents close to the synaptic input. For a thorough discussion of this *intrinsic dendritic filtering* effect and the consequences for the frequency content of measured LFP, see Linden et al. (2010) and Pettersen et al. (2012).

Figure 3.2 illustrates that while LFP might be a more local signal than EEG, it will generally be much more widespread than spikes. These typically spread less than 0.1 mm from the soma of the firing neuron (Holt and Koch 1999, Buzsaki 2004, Segev et al. 2004, Gold et al. 2006, Pettersen and Einevoll 2008, Pettersen et al. 2008). Further, the duration of spikes is so short that a recorded signal typically can be sorted into nonoverlapping spike contributions from individual neurons surrounding the electrode contact. In this context one may thus ask: How many neurons can an electrode record from? Since the individual neuronal contributions to the LFP extend much further both in time and space, the LFP cannot easily be dissolved into contributions from individual neurons in the same way. The LFP recorded by an electrode may in practice reflect activity from thousands of neurons located in its vicinity, and a proper interpretation of the signal in terms of the underlying neural activity is not straightforward. We will return to this question in the next sections, but a key factor determining how local the LFP is, is obviously how steeply the single-neuron LFP contributions decay with distance from the neuron.

To investigate this we placed reconstructed morphologies of layer-3 pyramidal, layer-4 stellate, and layer-5 pyramidal cells (Mainen and Sejnowski 1996) at various distances from virtual recording electrodes and calculated how the amplitude $f(r)$ of the single-cell LFP contribution decays with distance (Linden et al. 2011). The result is shown in Figure 3.3. While the neuron in Figure 3.2 only receives a single synaptic input, we here consider the more realistic situation with numerous, spatially distributed synaptic inputs, either placed homogeneously over the whole dendritic structure or only on the apical or basal part of the dendrites, see caption of Figure 3.3 and Linden et al. (2011) for details.

A first observation from Figure 3.3 is that for all combinations of cell type, synaptic distribution and recording position the amplitude of the LFP contribution from a neuron placed sufficiently far away from the electrode decays as $1/r^2$ with radial electrode distance r . Far away, the LFP thus decays like the potential around a current dipole. This is as expected since the current dipole moment is the lowest nonzero multipole moment: it follows from the cable equation and Kirchhoff's current law that the monopole contribution must be zero (Linden et al. 2010, Pettersen et al. 2012). Closer to the cells, the decay is less steep: For electrodes at the same vertical depth as the neuronal soma, $f(r)$ is seen to approximately follow a $1/r^{1/2}$ law (Figure 3.3b,c), while for electrodes positioned above or below the soma $f(r)$ is almost flat for the smallest radial distances (Figure 3.3d). This latter observation can be understood on the basis of geometry: for horizontal distances r much smaller

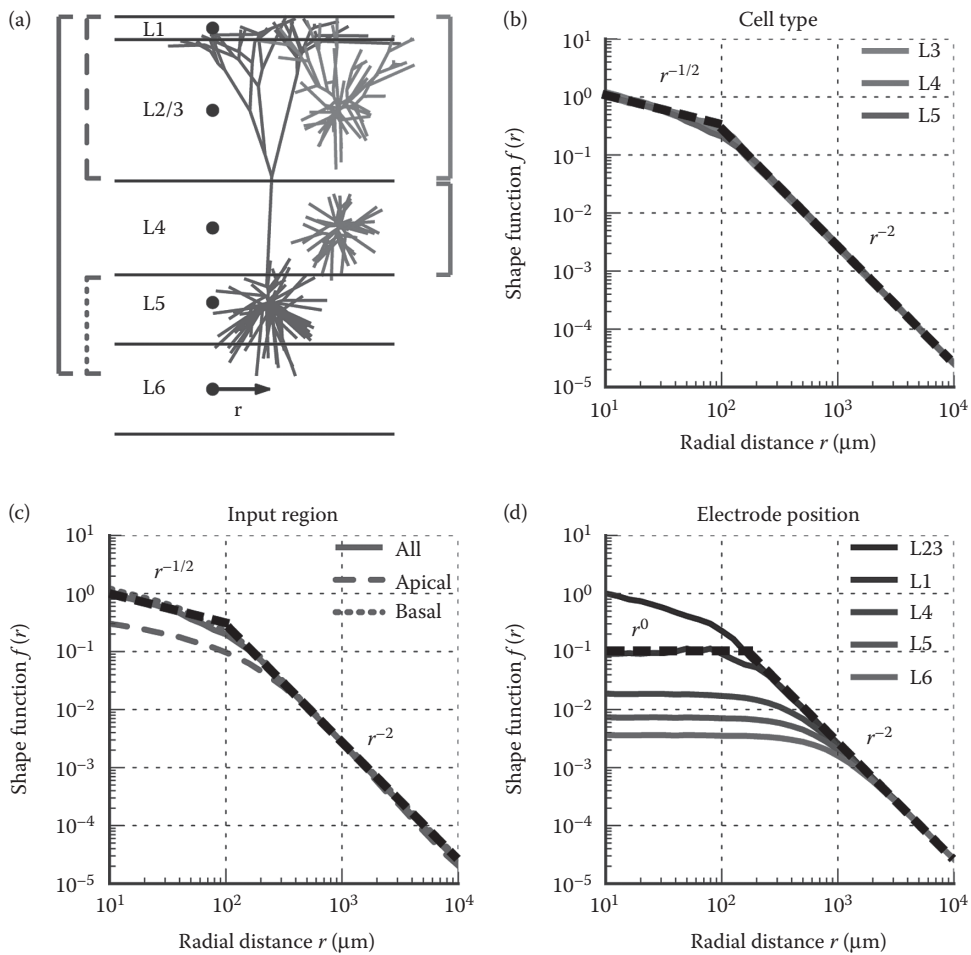


FIGURE 3.3 (See color insert.) Distance-dependence of amplitude of single-neuron contribution to the LFP. (a) Illustration of reconstructed cell morphologies used in simulations, layer-2/3 (L2/3) pyramidal cell (red), layer-4 (L4) stellate cell (green) layer-5 (L5) pyramidal cell (blue). Virtual electrode positions are shown as black dots. The single-cell LFP amplitude was calculated at different radial positions r as the average of the signal from 100 randomly rotated cells, each driven by 1000 uncorrelated Poissonian spike-trains with an individual firing rate of 5 spikes/s. The amplitude is here defined as the standard deviation of the LFP across time. The morphologies of these cells were randomly rotated along their vertical axis to introduce some heterogeneity, see Linden et al. (2011) for details. The shape function $f(r)$ describing the amplitude of single-cell LFP contributions, is calculated for cells receiving either homogenous (solid brackets), apical (dashed brackets) or basal (dotted brackets) synaptic input. (b) LFP amplitude for the three different cell types, recorded in the soma layer for each cell type. (c) LFP amplitude for L5 cell recorded in the L5 soma layer for different synapse distributions. (d) LFP amplitude at different recording depths for L2/3 cell receiving homogenous inputs. In (b)–(d), black dashed lines indicate decay proportional to various powers of r . Note that the timescale of these single-neuron LFPs is much longer than the timescale of the analogous extracellular potentials of action potentials depicted in the previous chapter. (Adapted from Linden et al. (2011).)

Q6

than the vertical distance between the neuron and the electrode, the distance from the neuron to the electrode will not change much when changing r .

These characteristic shapes of $f(r)$ suggest some simple approximate functional descriptions which will be used in the investigation of the LFP generated by populations of neurons in the next section. For the case where the electrode is at the same vertical depth as the soma, we assume:

$$f(r) = \begin{cases} f_0 & r < r_\epsilon \\ f_0(r_\epsilon/r)^{1/2} & r_\epsilon \leq r < r_x \\ f_0(r_\epsilon/r_x)^{1/2}(r_x/r)^2 & r \geq r_x, \end{cases} \quad (3.2)$$

see Figure 3.4a,c for illustration. Here r_x is the transition distance between the far-field dipole regime with a $1/r^2$ -decay and the slow-decay regime closer to the neurons. Interestingly, when the synapses are homogeneously distributed, r_x is seen to be about 0.1–0.2 mm for all three neurons (Figure 3.3b). However, r_x is seen to vary when the spatial distribution of the synapses over the dendrites are changed for the layer-5 pyramidal neuron (Figure 3.3c). We have further introduced a lower cut-off distance r_ϵ to avoid an unphysical divergence for $r \rightarrow 0$. This distance may, for example, correspond to the size of the neuronal soma, but we leave it unspecified as its specific value will have no consequence for the ensuing discussions.

For the situation when the electrode is above or below the depth of the soma, we correspondingly assume

$$f(r) = \begin{cases} f_0 & r < r_x \\ f_0(r_x/r)^2 & r \geq r_x, \end{cases} \quad (3.3)$$

which can be obtained by setting r_ϵ equal to r_x in Equation 3.2, see Figure 3.4b,d for illustration. In Figure 3.3d we observe a strong dependence of r_x on the vertical position. In particular, r_x increases with increased vertical distance between the neuron and electrode, again a feature that can be understood on the basis of simple geometric considerations (Linden et al. 2011).

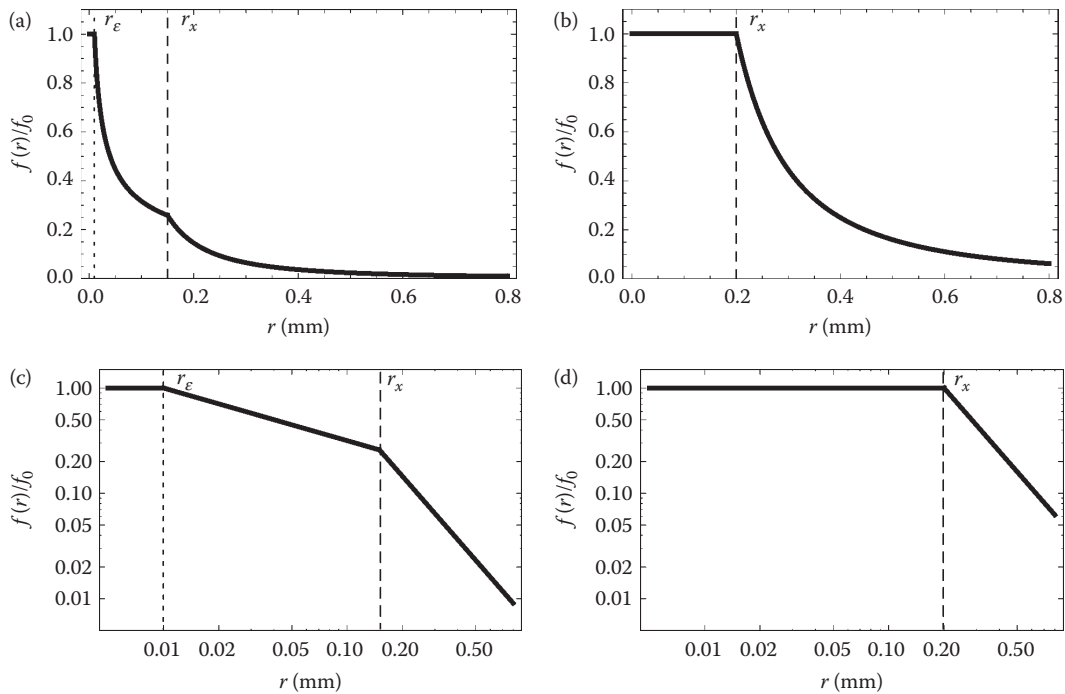


FIGURE 3.4 Illustration of phenomenological single-neuron shape functions $f(r)$ for the cases when (a) the electrode is at the same depth as the neuronal soma (Equation 3.2) and (b) when it is above or below (Equation 3.3). In (a) the parameters used are $r_x = 0.15$ mm, $r_\epsilon = 0.01$ mm, mimicking the situation in Figure 3.3b,c. In (b), $r_x = 0.2$ mm mimicking the situation for the layer-1 electrode in Figure 3.3d. Vertical dashed lines mark r_x , while vertical dotted lines mark r_ϵ . (c,d) Same as (a) and (b), respectively, in double-logarithmic plots.

3.4 POPULATION LFP

As the LFP recorded from an electrode in general stems from many neurons, an obvious question to ask is: *What is the size of the region generating the signal, that is, how local is the local field potential?* A neuron close to the electrode will obviously contribute more to the LFP than if the same neuron was located further away, as described by the function $f(r)$ in the previous section. However, as illustrated in Figure 3.5, it follows from the geometry of the situation that for a disc-like population with a homogeneous neuron density, the *number* of neurons located on a ring at a particular radial distance r will increase linearly with r . Thus, the relative contribution from different rings of neurons will depend on the competition between the decrease of the single-cell LFP amplitude with distance and the increase in the number of contributors with population size (Linden et al. 2011).

But there is also another factor that affects the locality of the measurement. Just as water waves from synchronized wave sources may interfere constructively to produce very large waves, signals from synchronized neuronal LFP sources may sum up to give much larger population LFPs than if they were unsynchronized. The summation of the contributions from the LFP sources in the vicinity of electrode, and also the question of locality of the LFP, will thus depend critically on how synchronous, or *correlated*, the signal from these sources are (Linden et al. 2011).

3.4.1 MODEL FOR POPULATION LFP

We now consider the formation of a compound LFP signal $\phi(t)$ from a disc-like population of radius R surrounding the electrode as illustrated in Figure 3.5. Following Linden et al. (2011) we assume that the contribution $\phi_i(t)$ from neuron i separates into a temporal and a spatial part,

$$\phi_i(t) = \xi_i(t) f(r_i) \quad (3.4)$$

where $f(r)$ is a shape function of the type described in Equations 3.2 and 3.3, and $\xi_i(t)$ is a time-dependent variable with zero mean and unit variance. If these single-neuron LFP contributions $\phi_i(t)$ are *uncorrelated*, that is, $\langle \phi_i(t) \phi_j(t) \rangle = 0$ for all $i \neq j$ where $\langle \cdot \rangle$ represent a temporal average, the variances from different neuronal LFP sources $\phi_i(t)$ add up linearly. The compound variance (power) is in the continuum limit then simply given by the integral

$$g_0(R) = \int_0^R dr N(r) f(r)^2 = \rho \int_0^R dr 2\pi r f(r)^2. \quad (3.5)$$

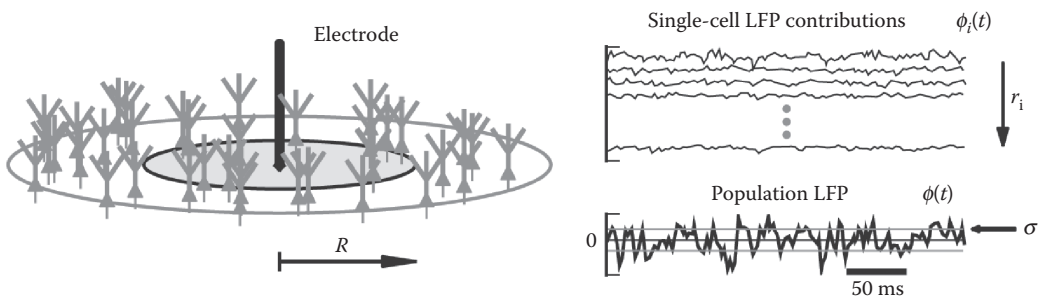


FIGURE 3.5 Sketch illustrating the generation of LFP from a population of identical neurons. Cells are homogeneously distributed on a disc of radius R with, in this case, the tip of the electrode in the center. The sum of LFP contributions $\phi_i(t)$ of individual cells at distances r_i from the population center results in a population LFP $\phi(t)$.

Here we have used that $N(r) dr = 2\pi r \rho dr$ is the number of neurons on the ring of radius r and width dr , where ρ is the area density of neuronal LFP sources. If, however, the single-neuron contributions $\phi_i(t)$ are completely *correlated*, that is, $\langle \phi_i(t) \phi_j(t) \rangle = \langle \xi_i(t) \xi_j(t) \rangle f(r_i) f(r_j) = f(r_i) f(r_j)$ for all i and j , the amplitudes of the LFP contributions add up, and the compound power is instead given by

$$g_1(R) = \left(\int_0^R dr N(r) f(r) \right)^2 = \rho^2 \left(\int_0^R dr 2\pi r f(r) \right)^2. \quad (3.6)$$

A more general expression for the compound LFP amplitude $\sigma(R)$ in the continuum limit, valid for arbitrary values of the pair-wise correlation $c_\phi = \langle \xi_i(t) \xi_j(t) \rangle$ (set to be identical for all pairs i, j), is given by (Linden et al. 2011)

$$\sigma(R) = \sqrt{(1 - c_\phi) g_0(R) + c_\phi g_1(R)}. \quad (3.7)$$

Our summation formulas for $g_0(R)$ and $g_1(R)$ in Equations 3.5 and 3.6 can be straightforwardly generalized to the situation where the electrode is not placed in the center of the circular population, but rather a distance X away (Linden et al. 2011):

$$\begin{aligned} g_0(R, X) &= \rho \int_{\{|r| \leq R\}} d^2r f(|\mathbf{r} - \mathbf{X}|)^2 \\ &= \rho \int_0^{2\pi} d\theta \int_0^R dr r f\left(\sqrt{(X - r \cos \theta)^2 + (r \sin \theta)^2}\right)^2, \end{aligned} \quad (3.8)$$

$$\begin{aligned} g_1(R, X) &= \left(\rho \int_{\{|r| \leq R\}} d^2r f(|\mathbf{r} - \mathbf{X}|) \right)^2 \\ &= \rho^2 \left(\int_0^{2\pi} d\theta \int_0^R dr r f\left(\sqrt{(X - r \cos \theta)^2 + (r \sin \theta)^2}\right) \right)^2. \end{aligned} \quad (3.9)$$

Here \mathbf{X} is the vector $X \mathbf{e}_x$, with \mathbf{e}_x being a unit vector in the x -direction. Equations 3.8 and 3.9 reduce trivially to Equations 3.5 and 3.6, respectively, when $X = 0$. For the intermediate case with some, but not complete correlation ($0 < c_\phi < 1$) the compound amplitude $\sigma(R, X)$ is found by replacing $g_0(R)$ and $g_1(R)$ with the functions $g_0(R, X)$ and $g_1(R, X)$, respectively, in Equation 3.7.

A notable difference between the uncorrelated ($g_0(R, X)$) and correlated ($g_1(R, X)$) contributions to the LFP power is that the former is proportional to area density ρ of neuronal LFP sources, while the latter is proportional to the *square* of ρ . So with everything else unchanged, the relative contribution from correlated sources compared to uncorrelated sources will increase when the density of neuronal sources is increased.

3.4.2 ANALYTICAL FORMULAS FOR SUMMATION OF POPULATION LFP

Population LFP amplitudes σ for arbitrary electrode positions (X , electrode depth), population sizes R , and correlation levels c_ϕ can now be found by insertion of the single-cell shape functions in Equations 3.2 (soma level) or (3.3) (above/below soma level) into Equations 3.5 through 3.9. For the

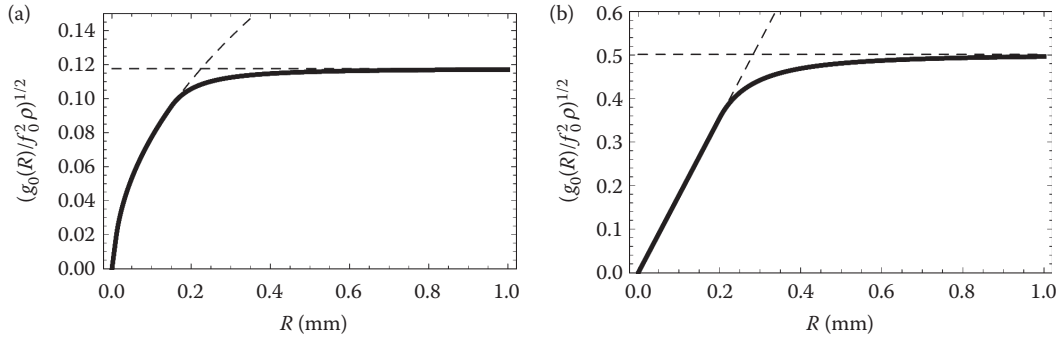


FIGURE 3.6 Illustration of how the LFP amplitude $\sigma(R)$ (Equation 3.7) grows with the size R of a disc-like population in the case of *uncorrelated* neuronal LFP sources, that is, $c_\phi = 0$. (a) Electrode at same depth as somas of neuronal population so that $\sigma(R) = (g_0(R))^{1/2}$, cf. Equation 3.10. Parameters used are $r_x = 0.15$ mm, $r_e = 0.01$ mm, mimicking the situation in Figure 3.3bc. The dashed lines represent the intermediate- R [$\sigma(R) = f_0 \rho^{1/2} (\pi r_e (2R - r_e))^{1/2}$] and large- R [$\sigma(R) = f_0 \rho^{1/2} (\pi r_e (3r_x - r_e))^{1/2}$] limits of $\sigma(R)$ in Equation 3.10. (b) Electrode above or below soma level, and $\sigma(R) = (g_0(R))^{1/2}$ is found by inserting $f(r)$ from Equation 3.3 into the integral expression in Equation 3.5. $r_x = 0.2$ mm to mimic the situation for the layer-1 electrode in Figure 3.3d. The dashed lines represent the intermediate- R [$\sigma(R) = f_0 \rho^{1/2} (\pi)^{1/2} R$] and large- R [$\sigma(R) = f_0 \rho^{1/2} (2\pi)^{1/2} r_x$] limits of $\sigma(R)$.

case where the electrode is centered in the population, one may even obtain analytical expressions. For electrodes *at* the soma level, one finds

$$g_0(R) = \begin{cases} f_0^2 \rho \pi R^2 & R \leq r_e, \\ f_0^2 \rho \pi r_e (2R - r_e) & r_e \leq R \leq r_x, \\ f_0^2 \rho \pi r_e (3r_x - r_e - r_x^3/R^2) & R \geq r_x, \end{cases} \quad (3.10)$$

$$g_1(R) = \begin{cases} f_0^2 \rho^2 \pi^2 R^4 & R \leq r_e, \\ f_0^2 \rho^2 \frac{1}{9} \pi^2 (r_e^2 - 4r_e^{1/2} R^{3/2})^2 & r_e \leq R \leq r_x, \\ f_0^2 \rho^2 \frac{1}{9} \pi^2 r_e (r_e^{3/2} - (4 + 6 \ln(R/r_x)) r_x^{3/2})^2 & R \geq r_x, \end{cases} \quad (3.11)$$

and analytical expressions for arbitrary values for the correlation c_ϕ can be found by insertion of these formulas into Equation 3.7. The corresponding results for the case when the electrode is above or below the soma level can be similarly obtained, but we do not list the formulas here. They can also be found by enforcing $r_e = r_x$ in the above equations. Numerical example results are plotted in Figure 3.6 for the case with uncorrelated neuronal LFP sources and in Figure 3.7 for correlated LFP sources.

3.4.2.1 Uncorrelated LFP Sources

We first focus on the case where the electrode is at the soma level for which we in Figure 3.6a observe that $\sigma(R)$ appears to converge to a finite value in the limit $R \rightarrow \infty$. This is confirmed by inspection of the analytical expression in Equation 3.10 where this limit value is seen to be $\sigma(R \rightarrow \infty) = (g_0(R \rightarrow \infty))^{1/2} = f_0 \rho^{1/2} (\pi r_e (3r_x - r_e))^{1/2}$ which gives $\sigma(R \rightarrow \infty) = 0.118 f_0 \rho^{1/2}$ for the numerical example in Figure 3.6a. The convergence of $\sigma(R)$ to a finite value suggests a definition of the *spatial reach* of the electrode as the population radius R_r at which the population amplitude has obtained a certain fraction α of the infinite-population value, that is, $\sigma(R = R_r) = \alpha \sigma(R \rightarrow \infty)$. In

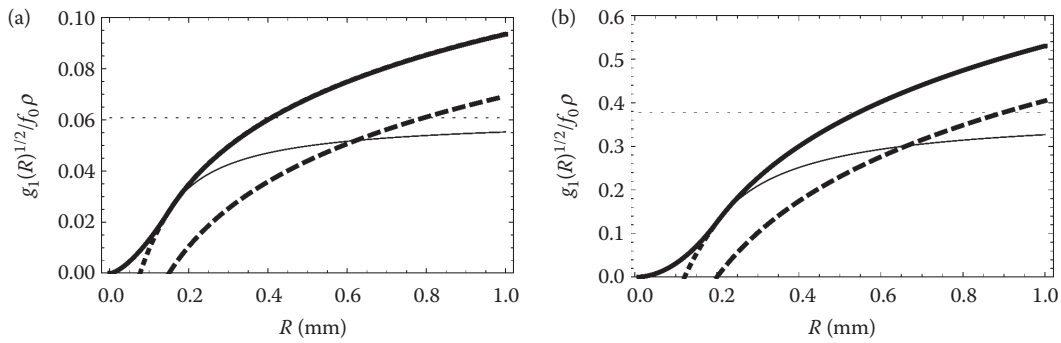


FIGURE 3.7 Illustration of how the LFP amplitude $\sigma(R)$ (Equation 3.7) grows with the size R of a disc-like population in the case of *correlated* neuronal LFP sources, that is, $c_\phi = 1$. (a) Electrode at the same depth as somas of neuronal population so that $\sigma(R) = g_1(R)$, cf. Equation 3.11 (thick solid line). Parameters used are $r_x = 0.15$ mm, $r_e = 0.01$ mm as before. Thick dashed line represents (extreme) large- R limit $[\sigma(R) = 2\pi f_0 \rho r_x^{3/2} \ln(R/r_x)]$, seen to parallel the true $\sigma(R)$ for large R with a constant shift. When including the constant term $[\sigma(R) = 2\pi f_0 \rho r_x^{1/2} r_x^{3/2} (\ln(R/r_x) + 2/3)]$, thick dotted line], the overlap with the true $\sigma(R)$ is essentially perfect for $R > 0.1$ mm. Corresponding result for $\sigma(R) = g_1(R)$ when the large-distance ($r > r_x$) decay of $f(r)$ in Equation 3.2 is assumed to go as $1/r^3$ instead of $1/r^2$, is shown with thin solid line, with the infinite- R limit indicated by the dotted horizontal line. (b) Electrode above or below soma level, and $\sigma(R) = g_1(R)$ is found by inserting $f(r)$ from Equation 3.3 into the integral expression in Equation 3.6. $r_x = 0.2$ mm as before. Thick dashed line represents (extreme) large- R limit $[\sigma(R) = 2^{1/2} \pi f_0 \rho r_x^2 \ln(R/r_x)]$, also seen to parallel the true $\sigma(R)$ for large R with a constant shift. When including a constant term that follows from the analytical evaluation of the integral for $g_1(R)$ $[\sigma(R) = 2^{1/2} \pi f_0 \rho r_x^2 (\ln(R/r_x) + 1/2)]$, thick dotted line], the overlap with the true $\sigma(R)$ is again essentially complete for $R > 0.15$ mm. Corresponding result for $\sigma(R) = g_1(R)$ when the large-distance ($r > r_x$) decay of $f(r)$ in Equation 3.3 is assumed to go as $1/r^3$ instead of $1/r^2$, is shown with thin solid line, with the infinite- R limit indicated by the thin dotted horizontal line.

Linden et al. (2011), we used such a definition with α set to 0.95. With the present analytical formulas for $\sigma(R)$ we may in a similar spirit define the spatial reach R_r as the population size at which the intermediate- R and large- R limits of $\sigma(R)$, that is, second and third lines in the piecewise defined function in Equation 3.10, cross each other. These limits are illustrated as dashed lines in Figure 3.6a, and from Equation 3.10 we find that R_r fulfills the equality $2R_r - r_e = 3r_x - r_e$, that is, $R_r = 1.5r_x$ independent of the value of r_e . Insertion into Equation 3.10 further shows that $\sigma(R_r = 1.5r_x)$ equals $(23/27)^{1/2} \sigma(R \rightarrow \infty)$ independent of the value for r_x (as long as $r_x \gg r_e$). As $(23/27)^{1/2} \approx 0.92$, a simple rule of thumb that emerges from our model is thus: *In the uncorrelated case 92% of the population LFP amplitude recorded by an electrode at the soma level stems from neurons closer than $R_r = 1.5r_x$.* In Figure 3.3 we found that for our example morphologies, r_x is about 0.15 mm, and in this case R_r is thus about 0.23 mm.

From this number for the spatial reach we can get a rough rule-of-thumb estimate for the number of neurons that can contribute to the LFP recorded at an electrode contact. Our modeling has focused on the two-dimensional case, that is, how the signal is built up by a disc-like population as the disc size increases. If we for simplicity assume a similar spatial reach when considering a volume of tissue surrounding the electrode contact, an estimate for the number of possibly contributing neurons can be found by counting the number of neurons inside a sphere of radius R_r : with a neuron density of, say, 50,000 neurons per mm^3 (Beaulieu 1993), a sphere of radius $R_r = 0.23$ mm will contain 2500 neurons.

Above we have focused on the situation with the electrode at the soma level, but the situation is qualitatively the same for the case where the electrode is above or below the soma, cf. Figure 3.6b. From simple analytical investigations (not shown here) it follows that here $\sigma(R \rightarrow \infty) = f_0 \rho^{1/2} (2\pi)^{1/2} r_x$, giving $\sigma(R \rightarrow \infty) = 0.50 f_0 \rho^{1/2}$ for the numerical example in Figure 3.6b. Further, the crossing of

the intermediate- R [$\sigma(R) = f_0 \rho^{1/2} \pi^{1/2} R$] and the large- R [$\sigma(R) = f_0 \rho^{1/2} (2\pi)^{1/2} r_x$] regimes occurs for $R_r = 2^{1/2} r_x \approx 1.4 r_x$ for which σ is found to be $3^{1/2}/2 \approx 0.87$ of $\sigma(R \rightarrow \infty)$.

3.4.2.2 Correlated LFP Sources

For the cases with correlated LFP sources in Figure 3.7 we observe that the LFP amplitude does not appear to saturate in the large-population limit (thick solid line). This is in accordance with the analytical expression in Equation 3.11 which shows a logarithmic divergence, that is, $\sigma(R) \approx \ln(R/r_x)$ for sufficiently large R . Thus, the simple conclusion is that regardless of electrode depth, the LFP will in principle be infinite if the electrode is surrounded by an infinite sea of correlated neuronal LFP sources when the contribution from each source decays as $1/r^2$ at large distances. From Equation 3.7 it is clear that this principal result pertains for all nonzero values of pair-wise correlations c_ϕ of the LFP contributions from individual neuronal sources.

In practice, of course, this divergence will not occur due to the necessarily finite size of pools of correlated neuronal LFP sources in the cortex, if for nothing else than due to the finite size of the brain. A more subtle effect that also would quench a divergence is that the vertical component of the current dipole may be expected to dominate the LFP from a population of pyramidal neurons, since the horizontal dipole components from the individual neuronal LFP sources will tend to average out (Linden et al. 2011). The contribution to the LFP from this vertical component will in the lateral direction effectively decay like $1/r^3$, not as $1/r^2$, for large distances (Pettersen and Einevoll 2008), and with such spatial decay the LFP signal will converge to a finite value even if the electrode is surrounded by an infinite sea of correlated neuronal LFP sources; see thin solid lines in Figure 3.7.

This reasoning about the hypothetical divergence of the LFP resembles the reasoning behind the interesting Olbers' paradox from astronomy regarding why the night sky is not completely illuminated by all the stars surrounding us, see Figure 3.8.

3.4.3 DECAY OF LFP OUTSIDE NEURONAL POPULATION

Another related question is how steeply the LFP from a neuronal population decays outside the population. We address this in our model by evaluating how the LFP amplitude measured by an electrode is reduced as the electrode is moved away from the center of the population. We denote the distance of the electrode from the population center by X , so that $X = R$ corresponds to the case where the electrode is positioned at the edge of the circular population. The LFP amplitude $\sigma(R, X)$ can be found by (i) evaluating the integral expressions $g_0(R, X)$ (Equation 3.8) and $g_1(R, X)$ (Equation 3.9) and (ii) inserting the results into the general relation for $\sigma(R, X)$ found by a simple modification of Equation 3.7, that is, $\sigma(R, X) = ((1 - c_\phi)g_0(R, X) + c_\phi g_1(R, X))^{1/2}$. In Figure 3.9 we show some example results for the two extreme cases: uncorrelated $c_\phi = 0$ ($\sigma(R, X) = g_0(R, X)^{1/2}$, panels A and C) or completely correlated $c_\phi = 1$ ($\sigma(R, X) = g_1(R, X)^{1/2}$, panels B and D). We here focus on the situation when the electrode is at same depth as the soma, since the LFP amplitude, that is, the value of f_0 , is much higher here than for the other electrode positions, cf. Figure 3.3 (see also Linden et al. 2011).

The solid lines in Figure 3.9 correspond to a case with a sizable neuronal population with a radius of $R = 1$ mm and the value $r_x = 0.15$ mm extracted from the single-cell shape functions in Figure 3.3. In this case we observe in panels A and B that the LFP amplitudes decay rapidly with X immediately outside the population. The decay length is essentially set by the value of r_x , as is confirmed by the corresponding results found when r_x is doubled to 0.3 mm (dotted lines): for this parameter set the decay with distance is seen to be less abrupt. The dashed curves correspond to the case when the population is very small, that is, $R = 0.2$ mm, which gives even more rounded curves and decays (when measured in terms of the relative off-center distance X/R), even with r_x set back to the default value of 0.15 mm.

When comparing the uncorrelated (panel A) and correlated cases (panel B), we observe that the relative reduction of the LFP at the population edge $X = R$ is larger for the correlated case than for



FIGURE 3.8 Why is the night sky dark? An interesting historical paradox from astronomy, known as Olbers' paradox (Harrison 1987), has some amusing analogies with the question of summation of LFP signals from many neurons. The question is why the night sky is dark given the following: (i) the light intensity from a single star falls off as $1/r^2$, (ii) in a homogeneous universe the number of stars in a spherical shell of a certain thickness around the Earth should increase as r^2 . According to this the contribution from each such shell of stars to the illumination on Earth should thus be independent of the distance r . With an infinite universe there will be an infinite number of shells and thus an infinite light intensity on Earth! This paradox is resolved if one takes into account modern knowledge that the universe is not infinitely old and the speed of light is finite so that there are no contributing stars for shells at distances of 14 billion light years or more away. This summation of light from numerous stars is analogous to the summation of LFP from numerous neurons in the surrounding brain. A difference is that while neuronal LFP generators are essentially dipoles, the stars are monopole light sources. Also the geometry is different (three-dimensional shells for stars, two-dimensional rings for neurons). The outcome is that while a finite universe is indeed required to resolve Olbers' paradox, an infinite brain may still give a finite LFP.

Q7

the uncorrelated case. This can be qualitatively understood by considering the special case $R \rightarrow \infty$ where being on the edge corresponds to being at the edge of an infinite half-plane. In this case the integral expressions in Equations 3.5 and 3.6 tell us that $\sigma(R, R)$ in the limit when $R \rightarrow \infty$ must approach $\sigma(R, 0)/2^{1/2}$ and $\sigma(R, 0)/2$ for the uncorrelated and correlated cases, respectively. Thus in this large-population limit, the LFP amplitude will be reduced to 0.5 of the maximal amplitude for the correlated case, but only to ≈ 0.7 of the maximal value for the uncorrelated case. For the numerical examples with $R = 1$ mm in Figure 3.9 we observe edge amplitudes close to these large- R predictions.

As illustrated by the double-logarithmic plots in Figures 3.9c and d, all LFP amplitude curves exhibit power-law behavior in the large- X limit, that is, when the electrode is moved far away from the active neuronal population. A closer analysis reveals a $1/X^2$ power law, the same as assumed in the single-cell shape function $f(r)$ in Equation 3.2. This can be understood by inspection of the integral expression for $g_0(R, X)$ (Equation 3.8) and $g_1(R, X)$ (Equation 3.9): when $X \gg R$, $f(|\mathbf{r}' - \mathbf{X}|)$ in the integrand can be approximated by $f(X)$ and moved outside the integral. It thus follows that the population inherits the single-neuron power law, as observed in Figure 3.9c and d. If a $1/r^3$ single-neuron large-distance power law had been assumed instead (as when moving laterally away from a vertical current dipole (Pettersen and Einevoll 2008), one would thus observe a $1/X^3$ decay.

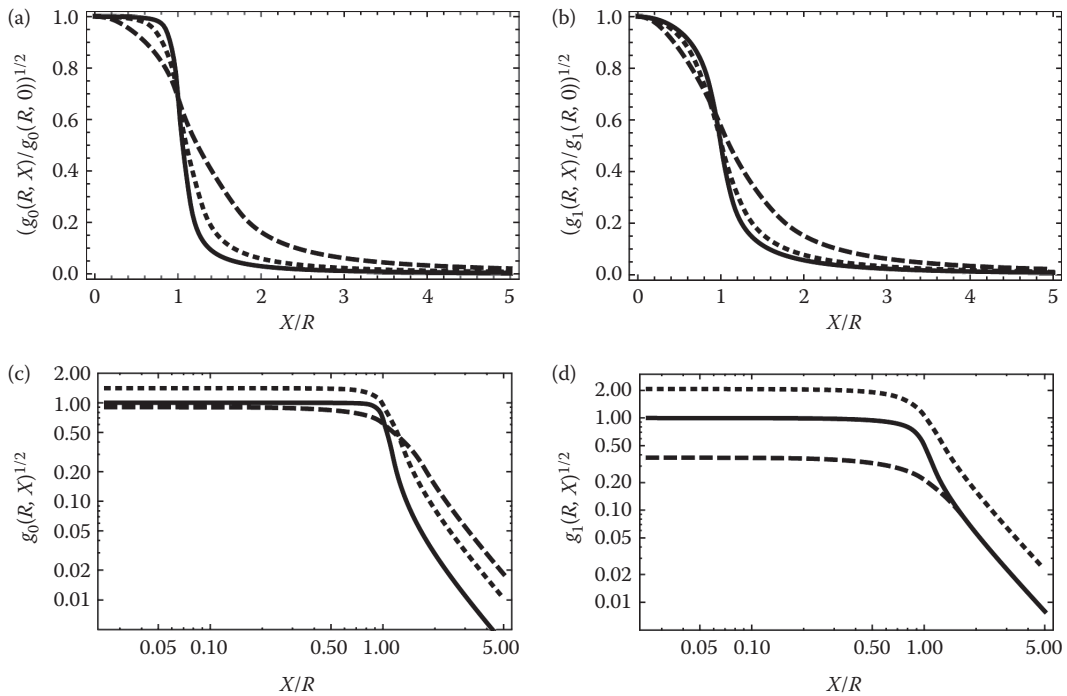


FIGURE 3.9 Example results showing how the LFP amplitude $\sigma(R, X)$ (Equation 3.7 with $g_0(R)$ and $g_1(R)$ replaced by $g_0(R, X)$ from Equation 3.8 and $g_1(R, X)$ from Equation 3.9, respectively) vary with electrode position X . (a) *Uncorrelated* population, that is, $c_\phi = 0$, so that $\sigma(R, X) = (g_0(R, X))^{1/2}$. (b) Completely *correlated* population, that is, $c_\phi = 0$, so that $\sigma(R, X) = (g_1(R, X))^{1/2}$. (c) Results in (a) shown in double-logarithmic plots. (d) Results in (b) shown in double-logarithmic plots. In all situations the electrode depth is set to the level of the neuronal soma, and $r_e = 0.01$ mm. Solid line: $R = 1$ mm, $r_x = 0.15$ mm. Dashed line: $R = 0.2$ mm, $r_x = 0.15$ mm. Dotted line: $R = 1$ mm, $r_x = 0.3$ mm. In (c) and (d), amplitudes are normalized relative to the response for a centered electrode for the case $R = 1$ mm, $r_x = 0.15$ mm.

Such a cubic power-law decay was in fact observed in comprehensive numerical simulations with pyramidal neurons receiving correlated synaptic inputs, when moving the electrode laterally outside populations, see Figure 3.7 in Linden et al. (2011).

Another observation in Figure 3.9d is that for the correlated situation with $X > \approx 1.5R$, the LFP only depends on the ratio X/R and r_x . This property can be seen directly by investigation of the integral expression for $g_1(R, X)$ in Equation 3.9 and the form of the large- R part of the single-cell shape function $f(r)$ in Equation 3.2.

3.5 ANALYSIS OF LFP DATA

3.5.1 CURRENT-SOURCE DENSITY (CSD)

As seen in Figure 3.9 in the previous section, the LFP from a synaptically activated neuronal population extends well beyond the dendrites of the active neurons themselves. To make the interpretation of recorded LFPs simpler it has thus been customary to estimate the so-called *current-source density* (CSD) thought to underlie the recordings (Pitts 1952, Freeman and Nicholson 1975). The CSD is a coarse-grained measure of the net volume density of transmembrane current entering or leaving the extracellular space as a function of position (Freeman and Nicholson 1975, Mitzdorf 1985) and will thus, unlike the LFP, be restricted spatially to the volume occupied by the dendrites of the active neurons.

The mathematical link between the CSD, here denoted by $C(\mathbf{r}, t)$, and the extracellular potential $\phi(\mathbf{r}, t)$ can be obtained directly by introducing $C(\mathbf{r}, t) = \sum I_n(t) \delta^3(\mathbf{r} - \mathbf{r}_n)$ in Equation 3.1 so that the equation can be transformed to

$$\phi(\mathbf{r}, t) = \frac{1}{4\pi\sigma_{ex}} \iiint_V \frac{C(\mathbf{r}', t)}{|\mathbf{r} - \mathbf{r}'|} d^3r'. \quad (3.12)$$

Here $\delta^3(\mathbf{r})$ is the three-dimensional Dirac δ -function, the volume integral goes over all transmembrane currents, and the quantity $C(\mathbf{r}, t)$ has dimension A/m³. (In general, $C(\mathbf{r}, t)$ will unlike the situation assumed in Equation 3.1 have contributions from many neurons.) A negative value of $C(\mathbf{r}, t)$ corresponds to current leaving the extracellular medium and is thus conventionally called a *sink*, while current entering the extracellular medium is called a *source*.

Equation 3.12 is a forward-modeling formula as it gives the mathematical recipe for calculating the extracellular potential when the CSD is known. A formula providing the opposite relationship can also be derived, and for the general case with a position-dependent extracellular conductivity $\sigma_{ex}(\mathbf{r})$ one has (Nicholson and Freeman 1975)

$$\nabla \cdot (\sigma_{ex}(\mathbf{r}) \nabla \phi(\mathbf{r}, t)) = -C(\mathbf{r}, t). \quad (3.13)$$

This equation in fact also applies when σ_{ex} depends on direction, for example, reflecting that it is easier for ions to move perpendicular to cortical layers than sideways (Goto et al. 2010), but in this case σ_{ex} will be a tensor (Nicholson and Freeman 1975). When σ_{ex} is isotropic and homogeneous, as assumed in Equation 3.1, the equation simplifies to

$$\sigma_{ex} \nabla^2 \phi(\mathbf{r}, t) = -C(\mathbf{r}, t) \quad (3.14)$$

known as the Poisson equation.

3.5.2 CURRENT-SOURCE DENSITY (CSD) ANALYSIS

We now turn to the practical problem of estimating the CSD from LFPs recorded by multielectrodes. A microscopic view into a piece of cortical tissue on the micrometer scale reveals that the dendrites, somas, and axons providing the transmembrane currents are entangled in a densely packed, spaghetti-like structure. Estimation of the detailed microscopic structure of transmembrane currents inside this spaghetti is out of the question with the present day multielectrodes used in *in vivo* preparations where a typical intercontact distance is 0.1 mm (Buzsaki et al. 2004). The CSD **Q1** is a more mesoscopic concept representing the average transmembrane current for a piece of neural tissue in a volume element a few tens of micrometers across, but in practice the spatial resolution of the estimated CSD will be poorer as it will be limited by the intercontact distances of the recording multielectrodes.

3.5.2.1 Traditional CSD Analysis

Traditional CSD analysis has been based on LFP recordings with linear (laminar) multielectrodes with equidistant electrode contacts inserted perpendicularly into the cortex or other laminarly oriented structures (Freeman and Nicholson 1975, Nicholson and Freeman 1975, Rappelsberger et al. 1981, Mitzdorf 1985, Di et al. 1990, Schroeder et al. 1998, 2001, Ulbert et al. 2001). The common assumption in the analysis has been that the variation in neural activation is so small in the lateral direction that only the variation of the potential ϕ in the vertical z direction needs to be considered, that is, $\phi(\mathbf{r}, t) = \phi(z, t)$. If so, the Poisson equation in Equation 3.14 simplifies to its one-dimensional

version:

$$\sigma_{ex} \frac{d^2 \phi(z, t)}{dz^2} = -C(z, t). \quad (3.15)$$

The discretized version of this equation has thus provided a natural choice for an estimator of the CSD: for depth position z_j the simplest choice for a CSD estimator $\hat{C}(z_j)$ is (Freeman and Nicholson 1975)

$$\hat{C}(z_j) = -\sigma_{ex} \frac{\phi(z_j + h) - 2\phi(z_j) + \phi(z_j - h)}{h^2}, \quad (3.16)$$

where h is the distance between adjacent electrode contacts. Other similar discrete filters have been used, often accompanied by additional spatial low-pass filters to remove noise (Freeman and Nicholson 1975, Ulbert et al. 2001). With N electrode contacts placed on a linear array, the estimator in Equation 3.16 predicts the CSD only at the $N-2$ interior contact positions (unless some additional assumptions are made regarding the LFP above and below the electrode, Vackin et al. 1988).

3.5.2.2 Inverse CSD Analysis

The assumption of a constant LFP in the direction perpendicular to the laminar electrode may clearly be problematic, for example, in sensory cortex where the stimulus-evoked activation patterns can be focused on a length scale of a few hundred micrometers (Swadlow et al. 2002, Pettersen et al. 2006, 2008, Einevoll et al. 2007, Jin et al. 2011, Hagen et al. 2011). This was noted already in the classical work by Nicholson and Freeman (1975) which demonstrated that small “columnar” activity diameters (≈ 1 mm or less) may give sizable errors in the estimated CSD and result in spurious predicted sinks and sources. One obvious remedy is to measure the extracellular potential in all three spatial directions and use a discretized version of the full Poisson equation in Equation 3.14 to construct an estimator akin to Equation 3.16 to estimate also the variation of the CSD in the lateral directions (Nicholson and Llinas 1975). However, such experiments are technically difficult to do, even if the new silicon-based multielectrodes offer new unprecedented possibilities (Buzsaki et al. 2004, Goto et al. 2010b, Leski et al. 2011).

In Pettersen et al. (2006) a new method, the *inverse CSD (iCSD)* method, was introduced to go beyond the limitations of traditional CSD analysis also when only one-dimensional LFP recordings are available. Similar in spirit to the inverse modeling approach to dipole source localization based on EEG data (He and Lian 2004), the iCSD method exploits the forward-modeling formula in Equation 3.12 to provide the appropriate CSD estimator. The core idea is straightforward: if we have LFP data recorded by a multielectrode with N contacts ($\{\phi_1, \phi_2, \dots, \phi_N\}$), a CSD distribution specified by N weight parameters ($\{C_1, C_2, \dots, C_N\}$) is constructed. The forward-modeling formula in Equation 3.12 can then be used to calculate the LFP set up by this CSD distribution at all N contacts. Due to the linearity of electrostatic theory, the relationship between these LFPs and the CSD can always be formulated in matrix form, that is,

$$\phi = \mathbf{FC}, \quad (3.17)$$

where $\phi = [\phi_1 \ \phi_2 \ \dots \ \phi_N]^T$ and $\mathbf{C} = [C_1 \ C_2 \ \dots \ C_N]^T$ are vectors containing the N recorded LFPs and the N parameters specifying the CSD, respectively. \mathbf{F} is an $N \times N$ matrix containing the forward-model link between the CSD and the LFP, as described by Equation 3.12. The N unknown CSD parameters, and thus the entire CSD distribution, can then be estimated from the N recorded potentials by

a matrix multiplication with the inverse matrix F^{-1} :

$$\hat{C} = F^{-1}\phi \quad (3.18)$$

There are of course many ways to specify a CSD distribution by means of N parameters, and in Pettersen et al. (2006) three variations of the method were considered, all assuming cylindrical symmetry in the underlying CSD activity: (i) the δ -source method where the CSD is assumed to be located in N infinitely thin, circular disks centered on the N electrode contacts of the laminar electrode, (ii) the *step* iCSD method, where the CSD instead is assumed to be step-wise constant in the z -direction, and (iii) the *spline* iCSD method based on cubic-splines interpolation. However, the estimated CSDs were found to be similar for the three methods (after suitable smoothing of the CSD estimates from δ -source and step methods to facilitate a comparison with the spline results).

The iCSD approach has several inherent advantages: First, *a priori* constraints such as knowledge about the lateral size of columnar activity and discontinuities or direction dependence of the extracellular conductivity, can be built directly into the iCSD estimator (Pettersen et al. 2006, Einevoll et al. 2007). When such information is lacking, for example on the lateral extent of CSD activity, a sensible analysis procedure is to do CSD estimation with the iCSD method assuming a range of values for the unknown parameters. This allows for more robustness in the CSD predictions, as features of the predicted CSD that are not robust to changes in the value of an *a priori* unknown parameter, cannot be trusted. With traditional CSD analysis, which corresponds to a special case of the iCSD method (Pettersen et al. 2006), such robustness testing is not possible.

Second, the iCSD method does not rely on a particular geometrical arrangement of the N electrode contacts recording the LFP signals. It is thus not only applicable to laminar multielectrodes (Pettersen et al. 2006), but also to other multielectrode geometries such as three-dimensional grids (Leski et al. 2007, Wojcik and Leski 2009) and multishank laminar electrodes providing a two-dimensional Cartesian grid of electrode contacts (Leski et al. 2011).

Third, unlike the traditional CSD method based on discretization of the Poisson equation in Equation 3.14, the iCSD method can also predict CSD at the positions of the boundary electrode contacts. With one-dimensional multielectrodes this may be a minor point as you only lose the prediction for 2 out of maybe 20 contact positions (Pettersen et al. 2006), but in, for example, three-dimensional recordings these boundary contacts may easily represent more than half of the total number of contacts (Leski et al. 2007).

A key element in practical use of the iCSD method will be testing of robustness to CSD predictions to *a priori* unknown parameters specifying the CSD distribution. In the one-dimensional iCSD method the diameter of the cylindrical activation and the conductivity jump at the cortical surface are two such parameters (Pettersen et al. 2006). In the two-dimensional iCSD method the main parameter is the thickness of the CSD activation in the direction perpendicular to the electrode grid (Leski et al. 2011). To facilitate easy testing of the effects of variation in these parameters, two easy-to-use, GUI-based MATLAB toolboxes have been made available at <http://software.incf.org/>: the toolbox “CSDplotter” for the case with one-dimensional multielectrodes and “iCSD 2D” for the case with multielectrodes forming a two-dimensional grid of contacts.

3.5.2.3 Other CSD Analysis Methods Based on Forward Model

Another recently developed method for CSD analysis is the *kernel CSD* (kCSD) method (Potworowski et al. 2012). It is a nonparametric method based on kernel techniques from machine learning. Unlike iCSD, the kCSD method does not require specification of an N -parameter family of CSD distributions. Rather, one can specify an arbitrarily large number of CSD sources, and the uniqueness of the CSD reconstruction is obtained from a minimum-norm regularization requirement inherent in the method. Therefore, the specification of the family of sources is decoupled from the arrangement of the recording grid, and a main practical advantage of the kCSD method is thus that it can be easily

applied to any geometrical arrangement of recording electrodes. While the iCSD in principle also may be modified to use with arbitrary arrangements of electrode contacts, the practical implementation of this may be cumbersome.

The latest contribution to the new host of forward-model-based CSD methods is the *volumetric CSD* (vCSD) method which was developed for analysis of LFP recordings with three-dimensional multielectrode recordings from the rat somatosensory cortex (Goto et al. 2010b).

3.5.3 INTERPRETATION IN TERMS OF NEURONAL POPULATIONS

While the CSD is a more local measure of neural activity and easier to interpret than the LFP, it does not directly tell us what neuronal populations are active and how the various populations drive each other synaptically. The CSD represents the net sum of transmembrane currents at a particular position, and in general several neuronal populations will contribute. For example, while an observed negative CSD (sink) in layer 2 may be due to currents going into dendrites of the basal region of layer-2 pyramidal neurons, it may equally well be due to currents going into the apical dendrites of layer-5 pyramidal cells, which also are present in this supragranular layer.

A natural goal is to go beyond CSD analysis and instead attempt to decompose the LFP and CSD into components from different laminar populations. Barth and coworkers pioneered this approach by using *principal components analysis* (PCA) on laminar data from rat somatosensory cortex and putatively identified two populations of pyramidal cells in the supragranular and infragranular layers, respectively (Di et al. 1990, Barth and Di 1991). A principal problem with this decomposition scheme, as for the more recent approaches using *independent component analysis* (ICA) (Makarov et al. 2010, Leski et al. 2010), is that the components are determined by purely mathematical constraints. For example, in PCA the spatiotemporal functions describing the activity in the various components are constrained to be mutually orthogonal (Gershenfeld 1999), while for ICA they are constrained to be statistically independent. It is, however, not clear how well the contributions to the CSD or LFP from the various neuronal populations actually satisfy these constraints.

In Einevoll et al. (2007) the so-called *laminar population analysis* (LPA) was introduced as an alternative method for decomposition of multielectrode signals into contributions from laminarly organized cortical populations. In LPA physiological constraints rather than somewhat arbitrary mathematical constraints, are used to decompose the signal into contributions from a set of populations. Unlike the PCA- and ICA-based approaches it requires access to both the low-frequency (LFP) and high-frequency (multi-unit activity, MUA) parts of the extracellular potential, and the key underlying assumption is that the measured LFP stems from postsynaptic subthreshold activity following action-potential firing in the same set of populations. This population firing activity is in turn measured by the MUA (Ulbert et al. 2001, Pettersen et al. 2008).

In Einevoll et al. (2007) LPA was applied to stimulus-averaged laminar-electrode data from barrel cortex of anesthetized rats after single whisker flicks, and the outcome of the analysis was threefold: (i) identification of the physiologically relevant laminar cortical populations in the barrel cortex and their vertical spatial position and extent, (ii) estimates of the firing rates of these populations, and (iii) estimates of the spatiotemporal LFP and CSD signatures after action-potential firing in the individual populations. While these *population CSDs* give more information about the underlying neural circuit activity than CSD analysis of the full LFP signal, they alone do not provide direct information on the synaptic connection pattern between the various identified populations. However, in combination with a template-fitting technique, based on LFP population templates calculated by means of Equation 3.1 using morphologically reconstructed neurons, a map of the functional synaptic connections between the identified populations could be estimated (Einevoll et al. 2007). The estimated population firing rates from barrel cortex was later used in combination with simultaneously recorded MUA from the homologous barreloid in thalamus driving the barrel column, to extract mathematical network models in terms of

population firing rates for the thalamocortical and intracortical signal processing in the whisker system (Blomquist et al. 2009).

A new approach for extraction of laminar population activity based on LFP recordings alone has recently been introduced (Gratiy et al. 2011). Taking advantage of the biophysical forward modeling scheme (Equation 3.1), assumed spatial correlations of synaptic inputs onto populations and/or *a priori* knowledge of synaptic connectivity, the method allows for reconstruction of population-specific synaptic input current profiles.

3.6 CONCLUDING REMARKS

The LFP has seen a revival in the recent years, in part due to rapid technological advances in multielectrode technology allowing for simultaneous measurement of LFP at many spatial positions. Compared to spikes, the extracellular signatures of action potentials, the LFP is despite its name inherently quite nonlocal. It is thus difficult to extract much useful information from single-electrode LFP recordings. On the other hand, it has been realized that the LFP signal, representing activity in populations of neurons, may contain a lot of information about the external world which is not readily available from the recorded spikes alone (Montemurro et al. 2008). There is thus an increasing need for methods for proper analysis of LFP data. This is also important in the context of development of brain–machine interfaces where the LFP signal has been suggested used in the steering of neuroprosthetic devices (Mehring et al. 2003, Andersen et al. 2004, Rickert et al. 2005).

Unlike other measurement modalities such as intrinsic optical imaging, two-photon calcium imaging or fMRI, the biophysics relating the neural activity to what is measured in electrical recordings is well understood (cf. Section 3.2). This is crucial as it allows for simultaneous forward modeling of, for example, spike trains and depth-resolved LFP from a candidate cortical network model, allowing for more comprehensive testing of such models against experiments. The long-term perspective should be that candidate network models should be tested against as many of the available experimental modalities as possible, for example, also the various optical imaging and magnetic resonance techniques. The theory making these links, that is, “the physics of neural activity measurements” (Brette and Destexhe 2012) and the neuroinformatics tools allowing for easy implementation of the calculation of these measurement modalities must thus be developed. For the LFP and MUA our group has, for example, developed a Python toolbox, *LFPy*, tailored for straight-forward simulations of extracellular potentials (Linden et al. 2011b). This toolbox runs on top of the NEURON simulator (<http://www.neuron.yale.edu/>) and uses standard data formats for neuronal morphologies allowing for easy use of morphological reconstructions available in online databases such as NeuroMorpho (<http://neuromorpho.org/>). Q8

The biophysical forward modeling scheme for LFP further allows for proper testing and correction of “folk-physics” interpretations of the LFP and CSD sometimes encountered in the field. An example is the incorrect notion that at an observed source in the CSD implies a hyperpolarization of the neurons, demonstrated in Figure 3.2 not to be generally true. This forward-modeling scheme using detailed reconstructed neuronal morphologies will also be invaluable in providing realistic ground-truth data for testing methods for analysis of LFP signals. This approach has already been used to validate the inverse CSD methods described in Section 3.5.2 (Pettersen et al. 2008, Leski et al. 2011). As the modeling scheme applies to spikes as well, it can also be used for generating ground-truth data to test LPA and the other methods for interpretation of multielectrode data outlined in Section 3.5.3 (Pettersen et al. 2008). The biophysical forward-modeling scheme based on Equation 3.1 which assumes a frequency-independent, isotropic and homogeneous electrical conductivity in the extracellular medium and a simple point-sized recording electrode, may if warranted be modified for improved accuracy (Pettersen et al. 2012). But it should be kept in mind that ground-truth test data do not have to be biophysically realistic in all ways in order to be useful. After all, if an aspiring data analysis method fails on relatively simple test data, it will be difficult to trust in an experimental setting. It should thus be a goal that all tools for analysis of data from electrical

recordings for which the forward solution is established, should be properly evaluated against test data for a host of different representative situations in which the method is used. For the related problem of validation of methods for automatic spike sorting, a coordinated collaborative effort to facilitate such validation is established (Einevoll et al. 2012; <http://www.g-node.org/spike>).

The LFP forward-modeling scheme described here can be straightforwardly modified to calculate EEG and MEG signals. In this case the recording devices are so distant from the neural sources that the dipole approximation can be used (Hamalainen et al. 1993, Linden et al. 2010). Further, the current dipoles set up by single neurons, and thus also populations of neurons, can be calculated directly based on the transmembrane currents in all neuronal compartments (Linden et al. 2010). The current dipole moment will in general depend on the neuronal morphology, spatial distribution of synaptic currents and frequency (Linden et al. 2010). For EEG recordings the electrical properties of dura matter, skull and scalp lying between the neural source and recording electrodes will influence the recorded signal, but these effects can be accounted for by applying modeling schemes already developed for EEG forward-modeling based on phenomenological mesoscopic current dipoles, for example, the three- or four-sphere model for electrical signal propagation in the head (Nunez and Srinivasan 2006). These modeling schemes may significantly improve the methodology in whole-brain simulators predicting EEG or MEG, as proper links between the quantities calculated in neural-field models and large-scale spiking neural-network models and their contribution to EEG and MEG signals can be developed (Bojak et al. 2010).

In this chapter, we have focused solely on how LFP is generated by neural activity and how measured LFP can be used to infer this underlying activity. The LFP may, however, feed back and affect the neural activity through what is known as ephaptic coupling, that is, by affecting the local value of the membrane potential felt by the ion channels (Anastassiou et al. 2011). As the LFP signal generally has amplitudes smaller than 1 mV (Kandel and Buzsaki 1997, Einevoll et al. 2007, Frohlich and McCormick 2010), this effect may *a priori* be expected to be small as the LFP-induced variation in the membrane potential will be small in absolute terms, that is, small compared to the difference between the resting potential and the threshold for spike initiations (~10–20 mV). However, even extracellular fields of this modest magnitude have in *in vitro* settings been seen to be sufficient to affect network activity and entrain spiking of action potentials (Frohlich and McCormick 2010, Anastassiou et al. 2011). The volume conductor theory underlying Equation 3.1 can also be used for mathematical modeling of such effects (Rattay 1986, Holt and Koch 1999).

ACKNOWLEDGMENTS

Numerous useful discussions with Anders M. Dale and Anna Devor on the neurophysiological significance of the extracellular potentials in general, and LFP in particular, are gratefully acknowledged. This work was supported by the Research Council of Norway (eVita, NOTUR, NevroNor, Yggdrasil) and the Polish–Norwegian Research Funding Mechanism.

REFERENCES

- Adrian H, Moruzzi G. 1939. Impulses in the pyramidal tract. *J Physiol (London)* 97:153–199.
- Anastassiou CA, Perin R, Markram H, Koch C. 2011. Ephaptic coupling of cortical neurons. *Nat Neurosci* 14:217–223.
- Andersen RA, Musallam S, Pesaran B. 2004. Selecting the signals for a brain–machine interface. *Curr Opin Neurobiol* 14:720–726.
- Avitan L, Teichler M, Abeles M. 2009. EEG generator—A model of potentials in a volume conductor. *J Neurophysiol* 102:3046–3059.
- Barth DS, Di S. 1991. Laminar excitability cycles in neocortex. *J Neurophysiol* 65:891–898.
- Beaulieu C. 1993. Numerical data on neocortical neurons in adult rat, with special reference to the GABA population. *Brain Res* 609:284–292.
- Berger H. 1929. Über das elektreenkephalogramm des menschen. *Arch Psychiatr Nervenkr* 87:527–570.

- Belitski A, Gretton A, Magri C, Murayama Y, Montemurro M, Logothetis N, Panzeri S. 2008. Low-frequency local field potentials and spikes in primary visual cortex convey independent visual information. *J Neurosci* 28:5696–5709.
- Blomquist P, Devor A, Indahl UG, Ulbert I, Einevoll GT, Dale AM. 2009. Estimation of thalamocortical and intracortical network models from joint thalamic single-electrode and cortical laminar-electrode recordings in the rat barrel system. *PLoS Comp Biol* 5:e1000328.
- Bojak I, Oostendorp TF, Reid AT, Kotter R. 2010. Connecting mean field models of neural activity to EEG and fMRI Data. *Brain Topogr* 23:139–149.
- Brette R, Destexhe A (eds). 2012. *Handbook of Neural Activity Measurements*. Cambridge University Press, Cambridge, UK.
- Buzsaki G. 2004. Large-scale recording of neuronal ensembles. *Nat Neurosci* 7:446–451.
- Caton R. 1875. The electric currents of the brain. *Br Med J* 2:278.
- Colgin LL, Denninger T, Fyhn M, Hafting T, Bonnevie T, Jensen O, Moser MB, Moser EI. 2009. Frequency of gamma oscillations routes flow of information in the hippocampus. *Nature* 462:353–357.
- Di S, Baumgartner C, Barth DS. 1990. Laminar analysis of extracellular field potentials in rat vibrissa/barrel cortex. *J Neurophysiol* 63:832–840.
- Einevoll GT, Pettersen KH, Devor A, Ulbert I, Hålgren E, Dale AM. 2007. Laminar population analysis: Estimating firing rates and evoked synaptic activity from multielectrode recordings in rat barrel cortex. *J Neurophysiol* 97:2174–2190.
- Einevoll GT, Felix Franke F, Hagen E, Pouzat C, Harris KD. 2012. Towards reliable spike-train recordings from thousands of neurons with multielectrodes. *Curr Opin Neurobiol* 22:11–17.
- Freeman JA, Nicholson C. 1975. Experimental optimization of current source-density technique for anuran cerebellum. *J Neurophysiol* 38:369–382.
- Frey U, Egert U, Heer F, Hafizovic S, Hierlemann A. 2009. Microelectronic system for high-resolution mapping of extracellular electric fields applied to brain slices. *Biosens Bioelec* 24:2191–2198.
- Frohlich F, McCormick D. 2010. Endogenous electric fields may guide neocortical network activity. *Neuron* 67:129–143.
- Gershenfeld N. 1999. *The Nature of Mathematical Modelling*. Cambridge University Press, Cambridge, UK.
- Gold C, Henze DA, Koch C, Buzsaki G. 2006. On the origin of the extracellular action potential waveform: A modeling study. *J Neurophysiol* 95:3113–3128.
- Gold C, Henze DA, Koch C. 2007. Using extracellular action potential recordings to constrain compartmental models. *J Comput Neurosci* 23:39–58.
- Goto T, Hatanaka R, Ogawa T, Sumiyoshi A, Riera J, Kawashima R. 2010. An evaluation of the conductivity profile in the somatosensory barrel cortex of Wistar rats. *J Neurophysiol* 104:3388–3412.
- Goto T, Ogawa T, Kawashima T, Riera J. 2010b. A volumetric current source density analysis with realistic geometrical properties and conductivity profiles in the somatosensory cortex of rats. *Proceedings of the 33rd Annual Meeting of the Japan Neuroscience Society*, P3-r10, Kobe, Japan, Sep 2010.
- Gratny SL, Devor A, Einevoll GT, Dale AM. 2011. On the estimation of population-specific synaptic currents from laminar multielectrode recordings. *Front Neuroinform* 5:32.
- Hagen E, Fossum JC, Pettersen KH, Alonso J-M, Swadlow HA, Einevoll GT. 2011. Modeling the LFP footprint of unitary thalamic inputs to sensory cortex. *BMC Neurosci* 12(Suppl 1):86 doi:10.1186/1471-2202-12-S1-P86.
- Hamalainen M, Hari R, Ilmoniemi R, Knuutila J, Lounasmaa O. 1993. Magnetoencephalography theory, instrumentation, and applications to noninvasive studies of the working human brain. *Rev Mod Phys* 65:413–497.
- Harrison E. 1989. *Darkness at Night: A Riddle of the Universe*. Harvard University Press, Cambridge, MA.
- He B and Lian J. 2004. Electrophysiological neuroimaging. In *Neural Engineering* (ed Bin He), Kluwer/Plenum, New York, NY.
- Henrie JA, Shapley R. 2005. LFP power spectra in V1 cortex: The graded effect of stimulus contrast. *J Neurophysiol* 94:479–490.
- Holt GR, Koch C. 1999. Electrical interactions via the extracellular potential near cell bodies. *J Comput Neurosci* 6:169–184.
- Jin J, Wang Y, Swadlow HA, Alonso JM. 2011. Population receptive fields of ON and OFF thalamic inputs to an orientation column in visual cortex. *Nat Neurosci* 14:232–238.
- Kandel A, Buzsaki G. 1997. Cellular-synaptic generation of sleep spindles, spike-and-wave discharges, and evoked thalamocortical responses in the neocortex of the rat. *J Neurosci* 17:6783–6797.
- Kreiman G, Hung CP, Kraskov A, Quiroga RQ, Poggio T, DiCarlo JJ. 2006. Object selectivity of local field potentials and spikes in the macaque inferior temporal cortex. *Neuron* 49:433–445.

- Lambacher A, Vitzthum V, Zeitler R, Eickenscheidt M, Eversmann B, Thewes R, Fromherz P. 2011. Identifying firing mammalian neurons in networks with high-resolution multi-transistor array (MTA). *Appl Phys A Mater Sci Process* 102:1–11.
- Leski S, Wojcik DK, Tereszczuk J, Swiejkowski DA, Kublik E, Wrobel A. 2007. Inverse current-source density method in 3D: Reconstruction fidelity, boundary effects, and influence of distant sources. *Neuroinformatics* 5:207–222.
- Leski S, Kublik E, Swiejkowski DA, Wrobel A, Wojcik DK. 2010. Extracting functional components of neural dynamics with independent component analysis and inverse current source density. *J Comput Neurosci* 29:459–473.
- Leski S, Pettersen KH, Tunstall, Einevoll GT, Gigg J, Wojcik DK. 2011. Inverse current source Density method in two dimensions: Inferring neural activation from multielectrode recordings. *Neuroinformatics* 9:401–425.
- Linden H, Pettersen KH, Einevoll GT. 2010. Intrinsic dendritic filtering gives low-pass power spectra of local field potentials. *J Comput Neurosci* 29:423–444.
- Linden H, Tetzlaff T, Potjans T, Pettersen KH, Gruen S, Diesmann M, Einevoll GT. 2011a. Modeling the spatial range of the LFP. *Neuron* 72:859–872.
- Linden H, Hagen E, Leski S, Norheim ES, Pettersen KH, Einevoll GT. 2011b. LFPy: A tool for simulation of extracellular potentials. Poster presented at “Neuroinformatics 2011”, Boston, USA (<http://www.neuroinformatics2011.org/abstracts/lfp-a-tool-for-simulation-of-extracellular-potentials>). Available from <http://software.incf.org/software/LFPy>.
- Liu J, Newsome WT. 2006. Local field potential in cortical area MT: Stimulus tuning and behavioral correlations. *J Neurosci* 26:7779–7790.
- Logothetis NK, Kayser C, Oeltermann A. 2007. *In vivo* measurement of cortical impedance spectrum in monkeys: Implications for signal propagation. *Neuron* 55:809–823.
- Mainen ZF, Sejnowski TJ. 1996. Influence of dendritic structure on firing pattern in model neocortical neurons. *Nature* 382:363–366.
- Makarov VA, Makarova J, Herreras O. 2010. Disentanglement of local field potential sources by independent component analysis. *J Comput Neurosci* 29:445–457.
- Mechler F, Victor JD. 2012. Dipole characterization of single neurons from their extracellular action potentials. *J Comput Neurosci* 32:73–100.
- Mehring C, Rickert J, Vaadia E, de Oliveira SC, Aertsen A, Rotter S. 2003. Inference of hand movements from local field potentials in monkey motor cortex. *Nat Neurosci* 6:1253–1254.
- Mitzdorf U. 1985. Current source-density method and application in cat cerebral cortex: Investigation of evoked potentials and EEG phenomena. *Physiol Rev* 65:37–100.
- Montemurro MA, Rasch MJ, Murayama Y, Logothetis NK, Panzeri S. 2008. Phase-of-firing coding of natural visual stimuli in primary visual cortex. *Curr Biol* 18:375–380.
- Montgomery SM, Buzsaki GM. 2007. Gamma oscillations dynamically couple hippocampal CA3 and CA1 regions during memory task performance. *Proc Natl Acad Sci USA* 104:14495–14500.
- Nicholson C, Freeman JA. 1975. Theory of current source-density analysis and determination of conductivity tensor for anuran cerebellum. *J Neurophysiol* 38:356–368.
- Nicholson C, Llinas R. 1971. Field potentials in the alligator cerebellum and theory of their relationship to Purkinje cell dendritic spikes. *J Neurophysiol* 34:509–531.
- Nicholson C, Llinas R. 1975. Real time current source-density analysis using multi-electrode array in cat cerebellum. *Brain Res* 100:418–424.
- Normann RA, Maynard EM, Rousche PJ, Warren DJ. 1999. A neural interface for a cortical vision prosthesis. *Vision Res* 39:2577–2587.
- Nunez PL, Srinivasan R. 2006. *Electric Fields of the Brain: The Neurophysics of EEG*. Oxford University Press, Oxford, UK.
- Pettersen KH, Devor A, Ulbert I, Dale AM, Einevoll GT. 2006. Current-source density estimation based on inversion of electrostatic forward solution: Effects of finite extent of neuronal activity and conductivity discontinuities. *J Neurosci Methods* 154:116–133.
- Pettersen KH, Einevoll GT. 2008. Amplitude variability and extracellular low-pass filtering of neuronal spikes. *Biophys J* 94:784–802.
- Pettersen KH, Hagen E, Einevoll GT. 2008. Estimation of population firing rates and current source densities from laminar electrode recordings. *J Comput Neurosci* 24:291–313.
- Pettersen KH, Linden, Dale AM, Einevoll GT. 2012. Extracellular spikes and CSD, In *Handbook of Neural Activity Measurements*, eds Brette R, Destexhe A, Cambridge University Press, Cambridge, UK.

- Pitts W. 1952. Investigation on synaptic transmission, in “Cybernetics”. New York: Trans. 9th Conf. Josiah Macy Found, pp. 159–166.
- Plonsey R, Barr RC. 2007. *Bioelectricity: A Quantitative Approach*. Springer, New York, NY.
- Potworowski J, Jakuczun W, Leski S, Wojcik DK. 2012. Kernel current source density method. *Neural Comput* 24:541–575.
- Rall W. 1962. Electrophysiology of a dendritic neuron model. *Biophys J* 2:145–167.
- Rappelsberger P, Pockberger H, Petsche H. 1981. Current source density analysis: Methods and application to simultaneously recorded field potentials of the rabbit’s visual cortex. *Pflügers Arch* 389:159–170.
- Rattay F. 1986. Analysis of models for external stimulation of axons. *IEEE Trans Biomed Eng* 33:974–977.
- Rickert J, de Oliveira SC, Vaadia E, Aertsen A, Rotter S, Mehring C. 2005. Encoding of movement direction in different frequency ranges of motor cortical local field potentials. *J Neurosci* 25:8815–8824.
- Roux S, MacKay WA, Riehle A. 2006. The pre-movement component of motor cortical local field potentials reflects the level of expectancy. *Behav Brain Res* 169:335–351.
- Scherberger H, Jarvis MR, Andersen RA. 2005. Cortical local field potential encodes movement intentions in the posterior parietal cortex. *Neuron* 46:347–354.
- Schroeder CE, Lindsley RW, Specht C, Marcovici A, Smiley JF, Javitt DC. 2001. Somatosensory input to auditory association cortex in the macaque monkey. *J Neurophysiol* 85:1322–1327.
- Schroeder CE, Mehta AD, Givre SJ. 1998. A spatiotemporal profile of visual system activation revealed by current source density analysis in the awake macaque. *Cereb Cortex* 8:575–592.
- Segev R, Goodhouse J, Puchalla J, Berry MJ. 2004. Recording spikes from a large fraction of the ganglion cell’s in a retinal patch. *Nat Neurosci* 7:1155–1162.
- Swadlow HA, Gusev AG, Bezdudnaya T. 2002. Activation of a cortical column by a thalamocortical impulse. *J Neurosci* 22:7766–7773.
- Szymanski FD, Garcia-Lazaro JA, Schnupp JW. 2009. Current source density profiles of stimulus-specific adaptation in rat auditory cortex. *J Neurophysiol* 102:1483–1490.
- Ulbert I, Halgren E, Heit G, Karmos G. 2001. Multiple microelectrode-recording system for human intracortical applications. *J Neurosci Methods* 106:69–79.
- Vaknin G, DiScenna PG, Teyler TJ. 1988. A method for calculating current source density (CSD) analysis without resorting to recording sites outside the sampling volume. *J Neurosci Methods* 24:131–135.
- Wojcik DK, Leski S. 2009. Current source density reconstruction from incomplete data. *Neural Comput* 22:48–60.
- Womelsdorf T, Fries P, Mitra PP, Desimone R. 2006. Gamma-band synchronization in visual cortex predicts speed of change detection. *Nature* 439:733–736.

Q10

TO: CORRESPONDING AUTHOR

AUTHOR QUERIES - TO BE ANSWERED BY THE AUTHOR

The following queries have arisen during the typesetting of your manuscript. Please answer these queries by marking the required corrections at the appropriate point in the text.

Query No.	Query	Response
Q1	The following references are not in the reference list: Pesaran et al. 2002, Buzsaki et al. 2004. Please provide complete publication details.	
Q2	Is it Liu et al. 2006 or Liu and Newsome 2006? Please confirm.	
Q3	Please specify Linden et al. 2011a or 2011b throughout this chapter.	
Q4	Is it Nunez and Srinivasan 2006 or Nunez and Srinavasan 2006? Please confirm the correct spelling.	
Q5	Is it Mechler and Victor 2011 or Mechler and Victor 2012? Please confirm the correct year.	
Q6	Please specify Linden et al. 2011a or 2011b.	
Q7	Is it Harrison 1987 or Harrison 1989? Please confirm the correct year.	
Q8	Please provide page number for the quote 'the physics of neural activity measurements'	
Q9	Please provide page number in Hagen et al. 2011.	
Q10	Plonsey and Barr, 2007 is not cited. Please suggest a suitable place for its citation in the text.	